This is the Pre-Published Version.

This is the accepted version of the following article: Liao, J., Jia, Y., Chen, L., Zhou, L., Li, Q., Qian, Z., ... & Li, P. (2019). Magnetic/gold core–shell hybrid particles for targeting and imaging-guided photothermal cancer therapy. Journal of Biomedical Nanotechnology, 15(10), 2072-2089, which has been published in https://doi.org/10.1166/jbn.2019.2839.

Magnetic/Gold Core-Shell Hybrid Particles for Targeting and Imaging-Guided Photothermal Cancer Therapy

Jinfeng Liao[1, 2], Yanpeng Jia[3], Lianghui Chen[1], Liangyu Zhou[1], Qiwen Li[2], Zhiyong Qian[3], Dechao Niu[4], Yongsheng Li[4], Pei Li[1*]

[1] Department of Applied Biology and Chemical Technology, The Hong Kong Polytechnic University, Hung Hom, Kowloon, Hong Kong, P. R. China
[2] State Key Laboratory of Oral Diseases, National Clinical Research Center for Oral Diseases, West China Hospital of Stomatology, Sichuan University, No. 14, Section 3, Southern Renmin Road, Chengdu 610041, Sichuan, P. R. China
[3] State Key Laboratory and Collaborative Innovation Center of Biotherapy, West China Hospital, Sichuan University, No. 17, Section 3, Southern Renmin Road, Chengdu 610041, Sichuan, P. R. China
[4] School of Materials Science and Engineering, East China University of Science and Technology, Shanghai, P. R. China

*** Corresponding author: Tel.: +852 34008721; Fax: +852 23649932; E-mail addresses:** pei.li@polyu.edu.hk (Pei Li)

Submitted date (Apr. 26, 2019)
Accepted date (May. 29, 2019)

Abstract

The development of hybrid particles for tumor diagnosis and therapy has received considerable attention because they are capable of combining tumor diagnosis and treatment concurrently. So far hybrid particles for efficient and safe tumor theranostics are still very limited. Herein we have designed a new type of hybrid particle and evaluated its potential to be used in image-guided cancer diagnosis and therapy without the need for any toxic anticancer or contrast agents. The hybrid particles consist of magnetic nanoparticles which are embedded in the poly(methyl methacrylate) (PMMA) cores and gold shells on chitosan (CTS) (γ-Fe_2O_3@PMMA/CTS@Au). The hybrid particles were synthesized through the initial formation of the core-shell structured γ-Fe_2O_3@PMMA/CTS particles containing approximately 20% loading of magnetic nanoparticles. A gold layer was then built on top of the core-shell magnetic particles *via* a reduction of gold salt by amines from the chitosan assisted with the reducing agent $NaBH_4$, followed by growing to complete gold shells in the presence of ascorbic acid (42.6% Au content). The properties of the composite particles including their chemical composition, morphology, particle size, size distribution, surface charge, magnetic responsiveness, and photothermal ability were systematically characterized. The potential application of the γ-Fe_2O_3@PMMA/CTS@Au hybrid particles in tumor diagnosis and therapy was assessed *in vitro* and *in vivo* using 4T1 tumor cells and 4T1 tumor-bearing mice through combining magnetic targeting, photoacoustic (PA)/computed tomography (CT) imaging and photothermal therapy. Results suggest that the γ-Fe_2O_3@PMMA/CTS@Au particles can serve as a multifunctional tumor theranostic nanoplatform for magnetically targeted photothermal therapy. Breast cancer has been effectively eliminated without the use of any anti-cancer drugs or contrast agents. Therefore, this type of core-shell hybrid particle represents a new composite particle design for effective and safe tumor theranostics.

Keywords: Multifunctional hybrid particles, magnetic targeting, photoacoustic imaging, CT imaging, photothermal therapy, tumor theranostics

1. INTRODUCTION

Breast cancer is a global health problem in women, accounting for 25% of deaths of all cancers in 2012 [1]. Unfortunately, the complex and heterogeneous nature of breast cancer makes its identification at the early stage difficult. In many cases, by the time breast cancer is diagnosed, it has already become aggressive and its rapid metastasis is the major cause leading to death [2-4]. With the rapid development of nanotechnology and nanobiomaterials, efficient tumor targeting, diagnosis, and therapy for cancer at the early stage have become possible [5-9]. Imaging technologies such as computed tomography (CT), magnetic resonance imaging (MRI), and ultrasonic imaging have been employed in cancer diagnosis to precisely locate tumors for accurate treatment. Nowadays, nanomaterial-based imaging is becoming more and more popular. In particular, gold nanoparticles have attracted considerable attention in photoacoustic (PA) imaging and CT imaging because of their unique physical, chemical, and biological properties [10-11]. The PA imaging technique possesses the advantages of both optical and acoustic methods. It has higher spatial resolution and deeper imaging depth than traditional optical imaging techniques. It also has better tissue contrast than ultra-sound imaging [12-13]. Meanwhile, CT imaging has its unique advantages such as deep penetration capability, great spatial resolution and density, and facile image reconstruction process. The contrast agents that are generally used in clinical practice are iodine-based small molecules (e.g., Omnipaque). They have some drawbacks such as non-specificity, short imaging time, and renal toxicity [14]. Since gold has a higher atomic number than iodine, gold nanoparticles show better X-ray attenuation property than iodine-based CT contrast agents [15-16]. Therefore, it is highly desirable to develop gold-based nanomaterials which have the advantages of both photoacoustic and CT imaging.

The photomediated therapeutic (PTT) approach is also one of the most promising choices for tumor therapy because it is a class of non-invasive therapeutic techniques. It has many advantages such as enhanced selectivity and low systemic toxicity, as well as being remote-controllable [17]. The efficacy of PTT has been significantly improved through the recent development of multifunctional nanocomposites based on gold nanoshells (GNS), gold nanorods (GNR), gold nanocages, graphene, single-walled carbon nanotubes, *etc* [18-20]. Compared with conventional chemotherapy which often results in poor therapeutic outcomes and serious side effects because of the non-targeting release of anticancer drugs *in vivo* and their low accumulation in tumor sites, the photomediated therapeutic approach has distinct advantages such as reduced toxic side effects and drug resistance [21-25]. Herein, we have designed a novel theranostic nanosystem that combines magnetic tumor targeting, photoacoustic/computed tomography imaging, and photothermal therapy (Scheme 1). The hybrid particles consist of magnetic nanoparticles embedded in the poly(methyl methacrylate) (PMMA) cores and gold shells on chitosan (CTS) (γ-Fe_2O_3@PMMA/CTS@Au). They have been constructed first through the synthesis of core-shell structured γ-Fe_2O_3@PMMA/CTS magnetic nanoparticles *via* surfactant-free emulsion polymerization, followed by the generation of gold nanoseeds on the chitosan shells by reducing the gold salt with amine groups of chitosan and $NaBH_4$ [26]. The gold nanoshell is further grown to form a complete shell over the surface of the γ-Fe_2O_3@PMMA/CTS particles in the presence of ascorbic acid, giving γ-Fe_2O_3@PMMA/CTS@Au core-shell hybrid particles (Fig. 1A.). Such an all-in-one theranostic nanoplatform is designed to simultaneously integrate magnetic targeting, PA imaging, CT imaging as well as photothermal therapy. To the best of our knowledge, no previous reports regarding the formation of γ-Fe_2O_3@PMMA/CTS@Au hybrid particles for dual-modal imaging and guided tumor-targeting therapy have been reported. Our theranostic nanoagent possesses three distinctive advantages: (1) The nanoagent contains high loading of iron oxide nanoparticles (up to 20%) which are covalently embedded in the inner core of the particle. The embedded magnetic nanoparticles are protected from the external environment, thus are much more stable than other magnetic nanoparticle systems that have been described in the literature [27-30]. (2) The gold nanoshell is formed over the surface of γ-Fe_2O_3@PMMA/CTS particles with a well-defined core-shell nanostructure. This kind of particle is very different from the previously reported gold nanoshell composite nanostructures such as SiO_2@Au [31-32], nanogel@Au [33], liposomes@Au [34], vesicle@Au [35], and Fe_3O_4@Au [36]. (3) The fabricated γ-Fe_2O_3@PMMA/CTS@Au hybrid particles are applicable for both PA and CT imaging with magnetic guided tumor targeting without the aid of any anti-cancer drugs [37] or imaging agents. Thus our theranostic nanosystem may be more efficient and safer for cancer therapy.

2. EXPERIMENTS

2.1. Materials and Instruments

Iron (II) chloride tetrahydrate ($FeCl_2·4H_2O$, Aldrich), anhydrous iron (III) chloride ($FeCl_3$, Fluka), ammonium hydroxide solution ($NH_3·H_2O$, 25 wt%, Aldrich), trisodium citrate dihydrate ($C_6H_5O_7Na_3·2H_2O$, SAFC), tetraethyl orthosilicate, [$Si(OC_2H_5)_4$, TEOS, International Laboratory USA], 3-(trimethoxysilyl)propyl methacrylate (MPS, Aldrich), chitosan of medium molecular weight (74% deacetylation, Aldrich), methanol (Lab-Scan) and ethanol (VWR) were used as received. Acid tetrachloroaurate (III) trihydrate ($HAuCl_4·3H_2O$), sodium borohydride ($NaBH_4$), L(+)-ascorbic acid (Vc), and thiolated polyethylene glycol ($mPEG_{5000}$-SH) were all purchased from Sigma-Aldrich, USA. Methyl methacrylate (MMA, Aldrich) was purified by washing three times with a sodium hydroxide solution (10 wt%), followed by washing with deionized water until the pH of the water layer dropped to 7. Deionized water (DI water) from the Milli-Q Gradient System was used in all experiments.

2.2. Synthesis of γ-Fe_2O_3@PMMA/CTS Composite Particles

The synthesis of γ-Fe_2O_3@PMMA/CTS particles was according to our previously established method [38-39]. Detailed experimental procedures for the preparation of citrate-coated γ-Fe_2O_3 nanoparticles (citrate-Fe_2O_3) and vinyl-coated γ-Fe_2O_3 nanoparticles (MPS-Fe_2O_3) can be referred to in our previous publications [39]. The preformed vinyl-coated γ-Fe_2O_3 nanoparticle dispersion (8.77 wt% in ethanol, 0.892

mL) was added dropwise to 44 mL chitosan solution (2.5 g chitosan dissolved in 220 mL of 0.6 v/v% acetic acid) and mixed with a homogenizer (6 w output) and a magnetic stirrer. After mixing for 30 min, the mixture (50 g) was transferred to a water-jacketed flask equipped with a magnetic stirrer, a condenser, and a nitrogen inlet. The mixture was degassed with nitrogen for 30 min at 80 ºC in the reactor. Purified MMA (0.638 mL) and H_2O_2 (0.051 mL, 100 mM) were added to the reaction flask. The reaction was continued at 80 ºC for 2 h, then stop by placing the pale yellow dispersion in an ice bath. The dispersion was purified by centrifugation at 18,000 rpm for 2 h three times. The final purified product was dispersed in water with a solids content of 0.635%.

The resultant particles were passed through a MACS LS magnetic column with a QuadroMACS Separator to separate those particles that contained few or no magnetic nanoparticles. The desired γ-Fe_2O_3@PMMA/CTS particles trapped by the magnetic column were released through washing with a 0.6% acetic acid solution without a magnetic field. The encapsulation efficiency was generally above 80% (The encapsulation efficiency = the amount of γ-Fe_2O_3@PMMA/CTS particles / (the amount of γ-Fe_2O_3@PMMA/CTS particles + the amount of PMMA/CTS nanoparticles without or low γ-Fe_2O_3).

2.3. The Preparation of γ-Fe_2O_3@PMMA/CTS@Au Hybrid Particles

Synthesis of γ-Fe_2O_3@PMMA/CTS@Au hybrid particles were synthesized according to the following procedure: 1) 5 mL of γ-Fe_2O_3@PMMA/CTS dispersion (6 mg/mL) was stirred with 93.2 μL 1% $HAuCl_4$ solution at 300 rpm for 30 min, followed by addition of 0.2 mL $NaBH_4$ solution (0.378 mg/mL). The mixture was further stirred for 24 h at room temperature to form gold nanoseeds over the surface of the γ-Fe_2O_3@PMMA/CTS particles. 2) The growth solution was prepared first: 50 mg K_2CO_3 was dissolved in 98 mL water under stirring for 30 min, followed by addition of 2 mL $HAuCl_4$ (0.025 M). The mixture initially appeared as a transparent yellowish solution, and slowly became colorless. The solution was allowed to stand for 24 h before usage. The above prepared γ-Fe_2O_3@PMMA/CTS@Au nanoseed dispersion (0.35 mL) was added to 18 mL water, followed by the addition of 12 mL growth solution under vigorously stirring. Subsequently, 240 μL (44 mg/mL) ascorbic acid (AA) solution was added to reduce the growth solution to form a gold shell. The solution turned to blue-green gradually. Finally, the hybrid particles were modified with a PEG-SH (2 mL, 10 mg/mL) to enhance the particle stability. The resultant dispersion was purified by centrifugation twice at 13,000 rpm for 10 min.

2.4. The Characterization of γ-Fe_2O_3@PMMA/CTS@Au Hybrid Particles

The dried samples including citrate-Fe_2O_3, MPS-Fe_2O_3, γ-Fe_2O_3@PMMA/CTS, and γ-Fe_2O_3@PMMA/CTS@Au particles were mixed with KBr, grounded to fine powders, then compressed into pellets. The FT-IR spectra were recorded in the transmission mode on a Nicolet Avatar 360 FT-IR spectrophotometer. UV-Vis absorption spectra were measured with a UV-Vis spectrophotometer (Agilent Technologies Cary 8454). The Scanning transmission electron microscopy (STEM, JEOL, JEM-2100F) with an accelerating voltage of 200 kV was used to observe particle morphology and conduct element analysis of the composite particles. The samples were prepared by adding a small drop of dilute particle dispersion (~500 ppm) onto a carbon-coated grid and drying it at room temperature. The hydrodynamic behavior of the hybrid particles in water was recorded by a Nanosight NS 300 instrument. The particle sizes and *zeta*-potentials of γ-Fe_2O_3@PMMA/CTS and γ-Fe_2O_3@PMMA/CTS@Au particles with concentrations of approximately 200 ppm were determined using a Zetasizer (Nano ZSP, Malven Instruments, England). The iron contents in the γ-Fe_2O_3@PMMA/CTS and the gold contents in the γ-Fe_2O_3@PMMA/CTS@Au particles were determined using a thermogravimetry analyzer [Thermogravimetry/differential scanning calorimeter (TGA/DSC3), Mettler Toledo]. The temperature was increased from 25 to 900 °C at a heating rate of 10 °C/min.

2.5. The Photothermal Analysis of the γ-Fe_2O_3@PMMA/CTS@Au Hybrid Particles

Different concentrations of γ-Fe_2O_3@PMMA/CTS@Au particles (50, 100, 200 and 300 μg/mL) were irradiated by an 808 nm laser (power density = 3.0 W/cm^2) for 5 min. Deionized water was used as a control sample. Temperature changes were recorded and near-infrared (NIR) images were captured using an Infrared (IR) thermal Fluke Ti32 camera (Infrared Cameras, USA).

2.6. *In vitro* Cytotoxicity

To study the cytotoxicity of γ-Fe_2O_3@PMMA/CTS@Au particles, 4T1 cells (a mouse breast cancer cell line) and NIH3T3 cells (a mouse embryonic fibroblast cell line) were cultured in the presence of the hybrid particles. Cells were seeded into a 96-well plate (5×10^3 cells/well, 100 μL), followed by incubating for 24 h. The old medium was replaced with a medium containing different dosages of γ-Fe_2O_3@PMMA/CTS@Au particles. Untreated cells in the growth media were used as the blank control. After 24 h of incubation, the cell viability was determined by the methylthiazolydiphenyl-tetrazolium bromide (MTT) assay.

2.7. Cell Viability after Photothermal Treatment

For cell viability measurements, 4T1 cells were plated into 96-well plates (5.0×10^3 cells/well) and allowed to adhere to the plate surface before the addition of 100 μg/mL γ-Fe_2O_3@PMMA/CTS@Au particles. The cells were then irradiated with an 808 nm NIR laser (power density = 3.0 W/cm^2) for 5 min. Subsequently, the cells were incubated for 24 h at 37 °C, followed by washing with PBS solution and fixing with 4% paraformaldehyde in PBS for 15 min. They were stained using LIVE/DEAD Cell Imaging Kit (Thermo Fisher Scientific Inc.) for 30 min, then washed by PBS, and imaged with a Leica TCS SP2 laser scanning confocal microscopy (CLSM, Leica Microsystem Inc., Germany). The cell survival percentage was calculated based on the average values of three random sections.

2.8. Systemic Toxicity of the γ-Fe_2O_3@PMMA/CTS@Au Particles

Female BALB/c mice (3 mice/group) were administered with saline and the γ-

Fe_2O_3@PMMA/CTS@Au (30 mg/kg) through a tail vein injection. Two weeks later, blood and serum samples were collected to evaluate the blood conditions and liver/kidney functions. Furthermore, mice were sacrificed to obtain their major organs (heart, lung, liver, spleen, and kidney) for toxicity analysis. Tissues were fixed with 10% formalin, embedded in paraffin, sectioned, and stained with hematoxylin and eosin (H&E).

2.9. *In vitro* and *in vivo* Photoacoustic Imaging

In vitro phantom imaging and *in vivo* photoacoustic (PA) imaging were carried out using a Multi-Spectral Optoacoustic Tomography (MSOT) imaging system (Vision 128, iThera medical, Germany). PA signals were acquired using a 128-element concave transducer array spanning a circular arc of 270° from 680 to 900 nm with an average pulse duration of about 10 ns and a repetition rate of 10 Hz. The transducer array has a central frequency of 5 MHz, which was used to provide a transverse spatial resolution of 150 μm. Image acquisition of samples was translated *via* the transducer array along its axis across the volume region of interest (ROI).

Phantom preparation and *in vitro* imaging: Cylindrical phantom with a diameter of 2 cm was prepared using both agar and intralipid. Briefly, 1.5 g of agar and 5 mL of 20% intralipid were added to 100 mL of deionized water and then heated to boiling. The mixture was filled into a 20 mL syringe after cooling. A straw (white plastic with an inner diameter of 2-3 mm) was cut to a length of 3-4 cm, and each side was sealed with glue. Two parallel straws in the center of the phantom were partially submerged and stabilized until the phantom solidified so that another straw containing the contrast agent could replace this air-filled straw. The phantom was imaged, while the straws were replaced in between scans. The concentrations of the γ-Fe_2O_3@PMMA/CTS@Au particles used for PA imaging phantom were 2.5, 5, 10, 20, 40, and 80 μg/mL.

In vivo PA imaging: The 4T1-bearing mice were intravenously injected with γ-Fe_2O_3@PMMA/CTS@Au dispersion (10 mg/kg). One group was treated with a magnetic field (MF) and another group without the magnetic field (3 mice/group). For *in vivo* PA imaging, the tumor-bearing mice were anesthetized with 3% isoflurane, and the anesthesia was maintained with 2% isoflurane. Subsequently, multi-wavelength PA imaging was carried out under the same condition with a step distance of about 0.3 mm along the long axis of the tumor. The maximum contrast of the PA signal was obtained when the excitation wavelength was at 700 nm during the PA imaging. Different time intervals of *in vivo* PA imaging were also studied.

2.10. Tumor Diagnosis Using CT Imaging

X-ray attenuation measurements*:* Different concentrations of γ-Fe_2O_3@PMMA/CTS@Au particles (0, 5, 7.5, 10, 15, and 20 mg/mL) were prepared. A common clinical agent, Iohexol, was used as the contrast. Samples of different concentrations (200 μL) were added to 1.5 mL Eppendorf tubes and CT scans

(Quantum GX, PerkinElmer) were performed at 90 kV and 80 μA with a slice of 0.02 mm thickness.

CT imaging *in vivo:* The 4T1-bearing mice were intravenously injected with γ-Fe_2O_3@PMMA/CTS@Au dispersion (10 mg/kg). One group was treated with the magnetic field and another group without the magnetic field (3 mice/group). For *in vivo* CT imaging, the mice were anesthetized. CT reconstruction images were then acquired before and after injection of γ-Fe_2O_3@PMMA/CTS@Au particles at the time points of 3, 6 and 24 h post-injection. Evaluation of X-ray attenuation intensity was carried out by loading the digital CT images in a standard display program, and then selecting a uniform region of interest on the resultant CT images. The CT value (Hounsfield units, HU) of each time point was collected from three sites of the tumor tissue. For the *in vivo* tumor CT imaging experiments, we used three tumor-bearing mice and selected the reconstruction images from one representative mouse.

2.11. *In vivo* Therapy of 4T1 Cancer-Bearing Balb/C Mice

All the animal procedures were carried out according to the guidelines on animal care in the State Key Laboratory of Biotherapy, Sichuan University, China. Female Balb/C mice (6 weeks old) were purchased from Beijing HFK Bioscience Co. Ltd, China. They were housed at temperatures between 20 and 22 °C with a relative humidity of 50-60% and 12-hour light-dark cycles. The mice were provided with free access to food and water. To induce breast cancer, 4T1 cells (1.0×10^6) were injected subcutaneously into the right rear flank area of the 8-week-old mice.

When the diameter of the tumor grew to approximately 5 mm, the tumor-bearing Balb/C mice were randomly divided into six groups (5 mice/group). The groups were treated with normal saline (group a), normal saline+Laser (group b), γ-Fe_2O_3@PMMA/CTS@Au (group c), γ-Fe_2O_3@PMMA/CTS@Au+MF (group d, MF: magnetic field), γ-Fe_2O_3@PMMA/CTS@Au+Laser (group e), or γ-Fe_2O_3@PMMA/CTS@Au+MF+Laser (group f). After intravenous injection of γ-Fe_2O_3@PMMA/CTS@Au dispersion (20 mg/kg), the tumors underwent external MF targeting for 24 h. Next, the tumor on each laser group mouse was irradiated by an 808 nm NIR laser at a power density of 3.0 W/cm^2 for 5 min and simultaneously imaged by an Infrared (IR) thermal Fluke Ti32 camera (Infrared Cameras, USA). A digital camera was used to take pictures of the mice at different times to observe the tumor growth. The weight of the mice and its tumor size were measured every other day. The tumor size was calculated based on the following equation: Volume = (Tumor Length) × (Tumor Width)^2/2. After different treatments of the tumor-bearing mice, the *ex vivo* lung tissues and tumors were further used for H&E staining.

3. RESULTS AND DISCUSSION

3.1. Synthesis and Characterization of γ-Fe_2O_3@PMMA/CTS@Au Hybrid Particles

Fig. 1A illustrates the synthesis of the γ-Fe_2O_3@PMMA/CTS@Au hybrid particles. The magnetic core-shell particles (γ-Fe_2O_3@PMMA/CTS) were first prepared through the emulsion polymerization of chitosan, methyl methacrylate (MMA), and vinyl-coated magnetic nanoparticles based on our previously established method [38, 39]. They were then coated with gold shells *via* the reduction of gold salt by amines from chitosan and the reducing agent $NaBH_4$ to form gold-seeded γ-Fe_2O_3@PMMA/CTS particles. The reduction of gold salt with amino groups of the chitosan layer involved an electrostatic interaction between the positively charged amine groups and the negatively charged gold complexes. This interaction attracted the gold salts into the chitosan shells where highly concentrated primary amines could reduce Au^{3+} to Au^0 *via* an electron transfer reaction. This reaction has been reported in our previous paper [26]. The gold seeds formed on the chitosan shell were further grown to a complete gold shell in the presence of ascorbic acid. The resultant γ-Fe_2O_3@PMMA/CTS@Au particles were further modified with thiolated polyethylene glycol ($mPEG_{5000}$-SH) to enhance their stability in water. Fig. 2B shows the FT-IR spectra of citrate-Fe_2O_3, MPS-Fe_2O_3, γ-Fe_2O_3@PMMA/CTS, and γ-Fe_2O_3@PMMA/CTS@Au particles. Characteristic absorption bands of Fe-O at 550~760 cm^{-1} were observed in all samples. The spectrum of citrate-Fe_2O_3 displays two broad absorption bands of the carboxylic group at ~1618 cm^{-1} (asymmetric) and ~1382 cm^{-1} (symmetric) stretching. The spectrum of MPS-Fe_2O_3 nanoparticles shows stretching vibration of C=O (~1726 cm^{-1}), C=C (~1637 cm^{-1}), and Si-O (~1150 cm^{-1}), indicating that the MPS molecules have been grafted onto the surface of the citrate-Fe_2O_3 nanoparticles. For the γ-

Fe_2O_3@PMMA/CTS particles, a strong peak at ~1731 cm^{-1} is the vibration of ester carboxyl group in PMMA. The C-O stretch is at 1250-1125 cm^{-1}. For γ-Fe_2O_3@PMMA/CTS@Au, an additional weak peak appeared at ~2360 cm^{-1} indicating the presence of a thiol group from the thiolated PEG. These representative peaks confirmed the successful synthesis of citrate-Fe_2O_3, MPS-Fe_2O_3, γ-Fe_2O_3@PMMA/CTS, and γ-Fe_2O_3@PMMA/CTS@Au particles. Scanning transmission electron microscopy (STEM) mapping images obtained with energy-dispersive X-ray spectroscopy (EDS) further confirmed the presence of Fe, Si, N, O, Au elements in the γ-Fe_2O_3@PMMA/CTS@Au particles (Fig. 2).

Fig. 1B(a) shows the morphology of the γ-Fe_2O_3@PMMA/CTS particles. Many magnetic nanoparticles with diameters less than 30 nm were embedded in the PMMA core. This type of particle was then used to form the γ-Fe_2O_3@PMMA/CTS@Au particles through the reduction of gold salt ($HAuCl_4 \cdot 3H_2O$) with the assistance of $NaBH_4$. Gold nanoparticles were first generated and spontaneously encapsulated by the chitosan shells. Fig. 1B(b) reveals the presence of gold nanoparticles (black dots) which are evenly distributed on the particle surface. To grow a complete gold shell on top of the particle, the gold-seeded nanoparticles were reduced with ascorbic acid in the presence of a growth solution. Fig. 1B(c) shows the morphology of resultantγ-Fe_2O_3@PMMA/CTS@Au particles which consist of magnetic nanoparticles in the cores and gold shells.

Hydrodynamic diameters and *zeta*-potentials of particles were measured by dynamic light scattering. The average particle sizes of γ-Fe_2O_3@PMMA/CTS, Au-seeded γ-Fe_2O_3@PMMA/CTS and γ-Fe_2O_3@PMMA/CTS@Au particles were 285.4 nm (PDI = 0.095), 234.7 nm (PDI = 0.108) and 228.1 nm (PDI = 0.205), respectively, [Fig. 1B(d)]. The reduction of average particle sizes of gold-modified nanoparticles was attributed to the strong binding of negatively charged gold nanoparticles with amine groups in chitosan, resulting in condensing the chitosan shell [26]. Therefore, the chitosan shell not only facilitates the formation of gold nanoseeds, but also provides particle stability during the modification procedures. The *zeta*-potential values were found to decrease from +47.2 mV to +22.3 mV after the forming of the γ-Fe_2O_3@PMMA/Au@CTS particles [Fig. 1B(e)].

Fig. 3A shows that the resultant γ-Fe_2O_3@PMMA/CTS@Au particles have a broad and strong UV-Vis absorbance in the near-infrared region (600-900 nm). This property enables the hybrid particles to be used for photothermal therapy with the NIR laser irradiation. The content of Fe in γ-Fe_2O_3@PMMA/CTS and that of Au in γ-Fe_2O_3@PMMA/CTS@Au particles were 20.9% and 42.6%, respectively, as determined by the thermogravimetry analyzer (Fig. 3B). Thus, the composition of the polymer in the hybrid particle was 36.5%. The magnetic properties including the hysteresis loop of γ-Fe_2O_3@PMMA/CTS have been determined in our previous study and showed excellent superparamagnetic property [39]. The magnetic responsiveness of both γ-Fe_2O_3@PMMA/CTS and γ-Fe_2O_3@PMMA/CTS@Au hybrid particles in water was demonstrated by placing a magnet next to the samples. Fig. 3C shows that both types of hybrid particles were effectively attracted to the side near the external magnet, and both could easily re-disperse in water. Furthermore, Fig. 3D illustrates that the PEGylated γ-Fe_2O_3@PMMA/CTS@Au particles were stable in various physiological solutions including cell medium with or without 10% FBS, PBS, normal saline, and water. The color of particle dispersion in the cell medium changed to pink, due to the presence of serum. No precipitations were observed in all of the dispersing media. These results indicated that the PEGylated γ-Fe_2O_3@PMMA/CTS@Au particles had good stability in different media, and the hybrid particles were suitable for cell and animal studies.

3.2. Photothermal Ability of the γ-Fe_2O_3@PMMA/CTS@Au Hybrid Particles

The photothermal ability of the hybrid particles was evaluated by irradiating various concentrations of particles with an 808 nm laser (3 W/cm^2) for 5 min. Fig. 4A shows the photothermal heating curves of these samples as shown indicate that increasing the concentration of the particles could lead to higher temperature elevation. Fig. 4B shows changes in the temperature over a period of 5 minutes as a function of the concentration of the hybrid particles. Results indicated that the elevation of temperature strongly depended on the particle concentration. This effect was further confirmed by IR images of hybrid particle dispersions of various concentrations under laser irradiation (Fig. 4C). The hybrid particles at 300 μg/mL exhibited a remarkable increase in temperature to up to 58 °C within 5 minutes (Fig. 4D), while the temperature variation of water as the control was negligible under the same irradiation condition.

Fig. 4E indicates that the dispersion could gradually cool down to the initial temperature after the laser irradiation was turned off. We have also studied the effect of light on/off cycles on the dispersion containing 300 μg/mL γ-Fe_2O_3@PMMA/CTS@Au hybrid particles. Fig. 3F shows that the hybrid particles were able to undergo repeated heating and cooling cycles, and maintained the photothermal temperature at ~ 57 ºC. These results suggest that the hybrid particle is a promising photothermal agent for tumor therapy.

3.3. Cell Viability and Systemic Toxicity of the γ-Fe_2O_3@PMMA/CTS@Au Hybrid Particles

The 4T1 tumor cells and 3T3 normal cells were employed to evaluate the *in vitro* cytotoxicity of γ-Fe_2O_3@PMMA/CTS@Au particles using an MTT assay. Fig. 5A and 5B show the results of cell viability of the γ-Fe_2O_3@PMMA/CTS@Au particles with concentrations up to 100 μg/mL. The survival percentages of 4T1 and 3T3 cells were 82.5% and 75.5%, respectively, when compared with the control. These results suggest that the γ-Fe_2O_3@PMMA/CTS@Au particles have good cell compatibility for their biological application.

The potential toxic effects of nanomaterials are the major obstacle for their application in biomedicine. Thus, a detailed toxicological study was conducted to evaluate the *in vivo* toxicity of the γ-Fe_2O_3@PMMA/CTS@Au hybrid particles. Balb/C mice were injected with the γ-Fe_2O_3@PMMA/CTS@Au particles at a dosage of 30 mg/kg. The mice injected with normal saline were used as the control group. Neither death nor any other sign of apparent weakness was observed for those mice treated with the hybrid particles. Furthermore, when compared with the control group (Fig. 5C), no significant changes were found in those key hematological parameters including RBC (red blood cell), WBC (white blood cell), PLT (platelets), HGB (hemoglobin), MCV (mean corpuscular volume), MCH (mean corpuscular hemoglobin), MCHC (mean corpuscular hemoglobin concentration) and MPV (mean platelet volume).

Various blood biochemical parameters were also evaluated with particular emphasis on the function of the liver and kidney (Fig. 5D). The liver function markers such as ALT (alanine aminotransferase), AST (aspartate aminotransferase), ALP (alkaline phosphatase), and TP (total protein) were assessed systematically. No obvious hepatic toxicity induced by the treatment of γ-Fe_2O_3@PMMA/CTS@Au particles was found. Indicators of kidney functions such as UA (uric acid) and BUN (blood urea nitrogen) levels in the serum of the treated mice were also normal compared with the control group. The hematological and blood biochemistry data confirm that the γ-Fe_2O_3@PMMA/CTS@Au particles have very low toxicity. Thus they would be safe for use in *in vivo* study.

Furthermore, the histological assessment (Fig. 5E) of major organs (heart, lungs, liver, spleen, and kidneys) also confirmed the absence of pathological damage in the γ-Fe_2O_3@PMMA/CTS@Au treated group, as compared with the saline control group.

No tissue toxicity or visible differences were found with a relatively high dosage (30 mg/kg) of γ-Fe_2O_3@PMMA/CTS@Au particles.

3.4. Photoacoustic Imaging *in vitro* and *in vivo*

Owing to the high density and extinction coefficients of gold nanoshells, the γ-Fe_2O_3@PMMA/CTS@Au hybrid particles may be employed as a contrast agent for photoacoustic imaging (PA). We first evaluated the photoacoustic properties of the γ-Fe_2O_3@PMMA/CTS@Au particles in a tissue-mimicking phantom as shown in Fig. 6A. Typical images obtained after the identification of the spectral components are shown in Fig. 6B. The γ-Fe_2O_3@PMMA/CTS@Au particles displayed PA green color, while there were no significant PA signals in the control one. The signal became brighter with the increasing concentration of the hybrid particles. This concentration-dependent behavior was confirmed with increasing particle concentrations from 2.5 to 80 μg/mL, leading to the increase of the mean pixel intensities to 1.29x10^4, 2.84x10^4, 5.61x10^4, 11.96x10^4, 13.64x$10^{4,}$ and 27.67x10^4. (Fig. 5E). The results suggest that the PA signal performance of the γ-Fe_2O_3@PMMA/CTS@Au particles was good enough to be applied in *in vivo* PA imaging.

Subsequently, we carried out the *in vivo* MSOT imaging and monitored the accumulation behavior of the particles in the tumor site through magnetic targeting. Fig. 6C illustrates a cross-sectional scan (dash line) of the tumor-bearing mice to obtain the PA imaging. Images of the mice before injecting the hybrid particles were taken as the control. The mice were then intravenously injected with the γ-Fe_2O_3@PMMA/CTS@Au particles, and monitored at 3, 6 and 24 h. PA imaging of the mice before the injection showed that the microenvironment of the tumor region (blue color) was hypoxia (Fig. 6D). With prolonged time, the green PA signal became more and more obvious, which might indicate enhanced permeability and retention (EPR) accumulation of the particles at the tumor site. In particular, the group with magnetic targeting showed a brighter PA signal in the tumor region. The mean pixel intensity values in the groups with magnetic targeting and without magnetic targeting were 6.25×10^6 and 3.77×10^6, respectively (Fig. 6F). The significant variation indicating that the γ-Fe_2O_3@PMMA/CTS@Au particles played an important role in the magnetic targeting of the tumor. With an external magnetic field, a better accumulation of particles in tumor tissue took place. The magnetic targeting induced by the hybrid particles enabled us to carry out an effective *in vivo* study of tumor diagnosis and therapy.

3.5. Computed Tomography Imaging

Computer tomography (CT) imaging is a clinical diagnostic tool with the advantages of deep penetration depth and high resolution. Gold nanoparticles have attracted considerable attention in CT imaging due to the higher atomic number of gold than that of iodine, thus providing better X-ray attenuation property than the iodine-based CT contrast agents. To evaluate the potential CT imaging capability of the γ-

Fe_2O_3@PMMA/CTS@Au particles, X-ray attenuation measurements *in vitro* were initially performed. A common clinical CT contrast agent named "Iohexol" was used as the control. Fig. 7A shows that the brightness of the phantom CT images increases with increasing concentration of both the γ-Fe_2O_3@PMMA/CTS@Au particles and Inhexol. Linear curves of γ-Fe_2O_3@PMMA/CTS@Au and Iohexol were obtained (Fig. 7B) by plotting the attenuation intensities of both samples against their concentrations. Similar to the brightness mentioned above, the attenuation intensity increased along with the increasing concentration. Although the attenuation intensity of γ-Fe_2O_3@PMMA/CTS@Au was not as strong as that of the Iohexol, there were no significant differences in their values. These results suggest that the γ-Fe_2O_3@PMMA/CTS@Au hybrid particles could be used for CT imaging.

To further demonstrate the CT imaging ability of the γ-Fe_2O_3@PMMA/CTS@Au particles *in vivo*, the Hounsfield units (HU) of the particles were evaluated after injecting the particles into mice. Fig. 7C illustrates the tumor region of mice in CT reconstruction images. Fig. 7D displays the *in vivo* reconstruction of CT images of 4T1 tumor-bearing mice with or without magnetic targeting, and before and after administration of the γ-Fe_2O_3@PMMA/CTS@Au particles at time points of 3, 6, and 24 h post-injection. The tumor sites became more and more observable with longer post-injection time in both groups. The corresponding tumor regions of the mice exhibited a clear CT signal after 24 h post-injection. It was found that the CT values of the tumor site treated with magnetic targeting were much higher (HU=103) than that of the mice without magnetic targeting (HU=88) (Fig. 7E). These results demonstrate that the γ-Fe_2O_3@PMMA/CTS@Au particles are an efficient type of CT contrast agent for tumor imaging. The magnetic targeting could enhance the HU value due to efficient particle accumulation in the tumor region.

3.6. Photothermal Therapy of 4T1 Cells and Tumor-Bearing Balb/C Mice with Magnetic Targeting

The effects of different treatment methods including incubating with normal saline without laser, with laser, γ-Fe_2O_3@PMMA/CTS@Au with laser and γ-Fe_2O_3@PMMA/CTS@Au with both laser and magnet field were systematically investigated using 4T1 cells and staining with the LIVE/DEAD Cell Imaging Kit. Calcein AM and propidium iodide (PI) were used to stain live (green) and dead (red) cells, respectively. Fig. 8A shows that the 4T1 cells incubated with culture medium without laser or with a laser in the absence of hybrid particles remained alive. On the other hand, almost all 4T1 cells died after photothermal treatment using the γ-Fe_2O_3@PMMA/CTS@Au particles under magnetic field and the 808 nm laser irradiation. For quantitative analysis, the cell survival in the presence of γ-Fe_2O_3@PMMA/CTS@Au particles without external magnetic field was 65.6%, while it was only 2.8% under the external magnetic field. The cell viability in control group and laser treatment group was 98.6% and 98.3%, respectively. These results demonstrate effective tumor cell with the magnetic field enhanced PTT effect.

The effect of different treatment methods was also studied using tumor-bearing

Balb/C mice. Fig. 8B(a) shows the whole-body thermal images of all laser treated groups which were monitored by an infrared camera. After irradiating with an 808 nm laser ($3W/cm^2$) for 5 min, the control group with normal saline injection did not exhibit an obvious temperature changes at the tumor region, while Groups e (γ-Fe_2O_3@PMMA/CTS@Au+Laser) and f (γ-Fe_2O_3@PMMA/CTS@Au+MF+Laser) displayed a rapid temperature increase to above 50 ^{0}C within 1 minute. Fig. 8B(b) shows that the temperature of the tumor site in Group f could reach to above 60 ^{0}C, which was higher than that of Group e (~55 ^{0}C). The results indicate that the magnetic targeting of γ-Fe_2O_3@PMMA/CTS@Au particles leads to the effective temperature rise at the tumor site after laser irradiation.

To further assess the performance of the γ-Fe_2O_3@PMMA/CTS@Au particles in photothermal therapy, tumor growth in mice was systematically examined in mice. Fig. 8B(c) shows that the tumor sites left black scars in the groups of γ-Fe_2O_3@PMMA/CTS@Au+Laser (Group e) and γ-Fe_2O_3@PMMA/CTS@Au+MF+Laser (Group f) after treatment for 3 days. On the other hand, the control groups, namely the groups of normal saline (Group a), normal saline+Laser (Group b), γ-Fe_2O_3@PMMA/CTS@Au (Group c), and γ-Fe_2O_3@PMMA/CTS@Au+MF (group d) showed no significant differences in the tumor size. Moreover, mice in these groups all exhibited rapid tumor growth [Fig. 8B(d)]. These mice treated with Group e (γ-Fe_2O_3@PMMA/CTS@Au+Laser) had 80% tumor regrowth, which might be due to the incomplete tumor ablation. Fortunately, 80% of the mice in Group f (γ-Fe_2O_3@PMMA/CTS@Au+MF+Laser) showed no tumor recurrence, indicating a magnetic targeting enhanced tumor ablation. Results shown in Fig. 8B(f) indicated that the 4T1 tumor-bearing mice in Groups of a, b, c and d had subsequently died because of the tumor growth and metastasis. Fortunately, the mice in Groups e and f kept survived after photothermal therapy in 42 days due to the effective tumor elimination. Meanwhile, 40% of the mice in Group e died due to high regrowth rate (80%) of tumors. While in Group f, all mice survived within two months. The results suggest that magnetic targeting photothermal therapy with γ-Fe_2O_3@PMMA/CTS@Au particles can effectively destroy the tumor, leading to prolonging the life span of mice.

Body weight is another important parameter to evaluate the systemic biocompatibility of the material to the body. Fig. 8B(e) shows that there are almost no body weight changes in all groups, indicating that the γ-Fe_2O_3@PMMA/CTS@Au hybrid particles have no adverse side effects *in vivo*.

The histological results of tumors after different treatments for 2 days are shown in Fig. 8C. No gross necrosis in tumors was observed in Groups a, b, c, or d. In contrast, a large necrotic area was observed after photothermal treatment by γ-Fe_2O_3@PMMA/CTS@Au (Group e) for 48 h. By combining with magnetic targeting (Group f), most of the tumor cells disappeared and the densely packed tumor cells were destroyed, leading to a widened space between the dead cells. The photothermal treatment at above 50 °C caused acute hemorrhage and tumor necrosis, which occurred in both Groups e and f. The results suggest that the photothermal therapy by the γ-

Fe_2O_3@PMMA/CTS@Au particles can efficiently induce tumor cell necrosis and death *via* hemorrhage and protein inactivation.

To further identify the lung metastasis before mortem, the mice were sacrificed before diagnosis with CT imaging. Fig. 9A shows the 2D reconstruction images of 4T1 tumor-bearing mice from different groups. The white arrows indicate the location of the lung tumor masses of mice from Groups in a, b, c and d, while the mice from Groups e and f had kept the normal structure of their lungs intact. Fig. 9B illustrates the lung tissues obtained from mice in the different groups that were sacrificed after treatment for 28 days. The white arrows in the pictures indicate the tumor proliferation regions in the lung tissues. It is clear to observe that tumor metastasis had taken place in all treated groups except for Groups e and f. Meanwhile, the lungs in Group a, b, c, d, e were hyperemia and swelling, and showed brighter color as well as a bigger size than Group f. These results indicated that the lung in Group e was invaded in the initial stage. Thus, Group f (γ-Fe_2O_3@PMMA/CTS@Au+MF+Laser) gave the best performance in tumor inhibition. Groups e and f had their normal structure of lungs remained intact, indicating that the photothermal therapy using γ-Fe_2O_3@PMMA/CTS@Au particles could efficiently inhibit tumor growth. Fig. 9C shows the histological results of the lungs of the different groups. No metastatic cancer cells were found in the lungs of Groups e and f. However, the other four groups (Groups a, b, c, and d) possessed abnormal structure of lungs. The white arrows indicated the tumor metastasis regions. The small cavities of alveoli in the lungs mostly disappeared and were occupied by tumor nodules. As a result, the mice might encounter breathing problem. Thus, the major cause of death of the tumor-bearing mice may be attributed to difficulty in breathing due to tumor metastasis in the lungs.

4. CONCLUSIONS

In summary, we have successfully fabricated the γ-Fe_2O_3@PMMA/CTS@Au core-shell hybrid nanoparticles and systematically evaluated their potential as a novel multifunctional cancer theranostic platform. The hybrid particles consist of 20.9% γ-Fe_2O_3 nanoparticles in the core, 42.6% gold shell, and 36.5% biocompatible polymers. They possess a highly uniform particle size distribution with an average diameter of 228.1 nm (PDI = 0.205) and a *zeta*-potential of +22.3 mV. The hybrid particles at 300 μg/mL exhibited remarkable temperature increase to up to 58 °C within 5 minutes. They can undergo repeated heating and cooling cycles, and maintained the photothermal temperature at ~ 57 °C. Cytotoxicity of the hybrid particles has been assessed through cell viability and systemic toxicity studies. Very low toxicity has been found both *in vitro* and *in vivo*. The capabilities of the hybrid particles as a contrast agent for photoacoustic and CT imaging have been evaluated under different treatment conditions. A combination of the hybrid particles with magnetic targeting and laser irradiation has given the optimal treatment outcome. Finally, photothermal therapies of 4T1 cells and tumor-bearing Balb/C mice have been investigated. Based on the excellent performance of using γ-Fe_2O_3@PMMA/CTS@Au hybrid particles in magnetic targeted photothermal therapy, the breast cancer was able to effectively eliminated without the use of any anticancer drug or contrast agent. Therefore, we conclude that the γ-Fe_2O_3@PMMA/CTS@Au core-shell hybrid particle is a promising agent for achieving efficient, safe, and imaging-guided tumor theranostics.

Acknowledgments

This work was financially supported by the Hong Kong Scholars Program (2016, XJ2016047), China Postdoctoral Science Foundation (0082204153001/003), NSFC/RGC Joint Research Scheme (N_PolyU533/14), and the PolyU Lo Ka Chung Centre for Natural Anti-Cancer Drug Development.

References and Notes

1. Ferlay, J., Steliarova-Foucher, E., Lortet-Tieulent, J., Rosso, S., Coebergh, J. W., Comber, H., Forman, D., Bray, F., **2013**. Cancer incidence and mortality patterns in Europe: estimates for 40 countries in 2012. *European Journal of Cancer,* 49(6), pp.1374-1403.
2. Shaheed, S., Tait, C., Kyriacou, K., Linforth, R., Salhab, M., Sutton, C., **2018**. Evaluation of nipple aspirate fluid as a diagnostic tool for early detection of breast cancer. *Clinical Proteomics,* 15, pp.3.
3. Pensabene, M., Stanzione, B., Cerillo, I., Ciancia, G., Cozzolino, I., Ruocco, R., Condello, C., Lorenzo, G. D., Giuliano, M., Forestieri, V., Arpino, G., Placido S. D., Lauria, R., **2018**. It is no longer the time to disregard thyroid metastases from breast cancer: a case report and review of the literature. *BMC Cancer,* 18, pp.146.
4. Sin, W. C., Lim, C. L., **2017**. Breast cancer stem cells-from origins to targeted therapy. *Stem Cell Investigation,* 4, pp.96.

5. Zhao, X., Yang, C. X., Chen, L. G., Yan, X. P., **2017**. Dual-stimuli responsive and reversibly activatable theranostic nanoprobe for precision tumor-targeting and fluorescence-guided photothermal therapy. *Nature Communication,* 8, pp.14998.

6. Shi, J., Kantoff, P. W., Wooster, R., Farokhzad, O. C., **2016**. Cancer nanomedicine: progress, challenges and opportunities. *Nat*ure *Rev*iew, 17, pp.20-37.

7. Tan, L. W., Ma, B. Y., Zhao, Q., Chen, L. J., Peng, J. R., Qian, Z. Y., **2017**. Toxicity evaluation and anti-tumor study of docetaxel loaded mPEG-polyester micelles for breast cancer therapy. *Journal of Biomedical Nanotechnology*, 13, pp.393-408.

8. Peng, J., Dong, M., Ran, B., Li, W., Hao, Y., Yang, Q., Tan, L., Shi, K., Qian, Z., **2017**. "One-for-all"-type, biodegradable prussian blue/manganese dioxide hybrid nanocrystal for trimodal imaging-guided photothermal therapy and oxygen regulation of breast cancer. *ACS Applied Materials &. Interfaces,* 9, pp.13875-13886.

9. Zhao, Hang., Wang, Y., Peng, J. R., Zhang, L., Qu, Y., Chu, B. Y., Dong, M. L., Tan, L. W., Qian, Z. Y., **2017**. Biodegradable self-assembled micelles based on MPEG-PTMC copolymer: an ideal drug delivery system for vincristine. *Journal of Biomedical Nanotechnology*, 13, pp.427-436.

10. Xiong, D., Zhang, X., Peng, S., Gub, H., Zhang, L., **2018**. Smart pH-sensitive micelles based on redox degradable polymers as DOX/GNPs carriers for controlled drug release and CT imaging. *Colloids and Surfaces B,* 163, pp.29-40.

11. Ruan, S., Hu, C., Tang, X., Cun, X., Xiao, W., Shi, K., He, Q., Gao, H., **2016**. Increased gold nanoparticle retention in brain tumors by in situ enzyme-induced aggregation. *ACS Nano* 10, pp.10086-10098.

12. Wu, B., Lu, S. T., Yu, H., Liao, R. -F., Li, H., Zafitatsimo, B.V. L., Li, Y. -S., Zhang, Y., Zhu, X. -Lei., Liu, H. -G., Xu, H. -B., Huang, S. -W., Cheng, Z., **2018**. Gadolinium-chelate functionalized bismuth nanotheranostic agent for in vivo MRI/CT/PAI imaging-guided photothermal cancer therapy. *Biomaterials,* 159, pp.37-47.

13. Neuschmelting, V., Kim, K., Malekzadeh-Najafabadi, J., Jebiwott, S., Prakash, J., Scherz, A., Coleman, J. A., Kircher, M. F., Ntziachristos, V., **2018**. WST11 vascular targeted photodynamic therapy effect monitoring by multispectral optoacoustic tomography (MSOT) in mice. *Theranostics,* 8(3), pp.723-734.

14. Hallouard, F., Anton, N., Choquet, P., Constantinesco, A., Vandamme, T., **2010**. Iodinated blood pool contrast media for preclinical X-ray imaging applications - a review. *Biomaterials,* 31, pp.6249-6268.

15. Wang, Z., Shao, D., Chang, Z., Lu, M., Wang, Y., Yue, J., Yang, D., Li, M., Xu, Q., Dong, W., **2017**. Janus gold nanoplatform for synergetic chemoradiotherapy and computed tomography imaging of hepatocellular carcinoma. *ACS Nano,* 11, pp.12732-12741.

16. Zhu, J., Sun, W., Zhang, J., Zhou, Y., Shen, M., Peng, C., Shi, X., **2017**. Facile formation of gold-nanoparticle-loaded γ-polyglutamic acid nanogels for tumor computed tomography imaging. *Bioconjugate Chemistry,* 28, pp.2692-2697.

17. Peng, J., Yang, Q., Li, W., Tan, L., Xiao, Y., Chen, L., Hao, Y., Qian, Z., **2017**. Erythrocyte-membrane-coated prussian blue/manganese dioxide nanoparticles as H_2O_2-responsive oxygen generators to enhance cancer chemotherapy/photothermal therapy. *ACS Applied Materials & Interfaces,* 9, pp.44410-44422.

18. Zhao, R., Han, X., Li, Y., Wang, H., Ji, T., Zhao, Y., Nie, G., **2017**. Photothermal effect enhanced cascade-targeting strategy for improved panceatic cancer therapy for improved pancreatic cancer therapy by gold nanoshell@mesoposous silica nanorod. *ACS Nano,* 11, pp.8103-8113.

19. Pan, L., Liu, J., Shi, J., ***2017***. Nuclear-targeting gold nanorods for extremely low NIR activated photothermal therapy. *ACS Applied Materials & Interfaces,* 9, pp.15952-15961.

20. Su, S., Wang, J., Vargas, E., Wei, J., Martínez-Zaguilán, R., Sennoune, S. R., Pantoya, M. L., Wang, S., Chaudhuri, J., Qiu, J., ***2016***. Porphyrin immobilized nanographene oxide for enhanced and targeted photothermal therapy of brain cancer. *ACS Biomaterials Science Engineering,* 2, pp.1357-1366.

21. Zhang, P., Huang, H., Huang. J., Chen, H., Wang. J., Qiu, K., Zhao, D., Ji, L., Chao, H., ***2015***. Noncovalent ruthenium(II) complexes-single-walled carbon nanotube composites for biomodal photothermal and photodynamic therapy with near-infrared irradiation. *ACS Applied Materials & Interfaces,* 7, pp.23278-23290.

22. Wang, H., Zhao, R., Li, Y., Liu, H., Li, F., Zhao, Y., Nie, G., ***2016***. Aspect ratios of gold nanoshell capsules mediated melanoma ablation by synergistic photothermal therapy and chemotherapy. *Nanomedicine,* 12, pp.439-448.

23. Yang, D., Yang, G., Yang, P., Lv, R., Gai, S., Li, C., He, F., Lin, J., ***2017***. Assembly of Au plasmonic photothermal agent and iron oxide nanoparticles on ultrathin black phosphorus for targeted photothermal and photodynamic cancer therapy. *Advanced Functional Materials,* 27, pp.1700371.

24. Wang, T., Wang, D., Yu, H., Wang, M., Liu, J., Feng, B., Zhou, F., Yin, Q., Zhang, Z., Huang, Y., Li, Y., **2016**. Intracellularly acid-switchable multifunctional micelles for combinational photo/chemotherapy of the drug-resistant tumor. *ACS Nano*, 10, pp.3496-3508.

25. Qu, Y., Chu, B. Y., Shi, K., Peng, J. R., Qian, Z. Y., **2017**. Recent progress in Functional micellar carriers with intrinsic therapeutic activities for anticancer drug delivery. *Journal of Biomedical Nanotechnology*, 13, pp.1598-1618.

26. Peter, N., Tan, B., Lee, C. H., Chen, L., Ho, K. M., Lu, Y., Ballauff, M., Li, P., **2015**. Facile synthesis of gold/polymer nanocomposite particles using polymeric amine-based particles as dual reductants and templates. *Polymer*, 76, pp.271.

27. Kim, J., Lee, J. E., Lee, S. H., Yu, Jung H. J., Lee, H., Park, T. G., Hyeon, T., **2008**. Designed fabrication of a multifunctional polymer nanomedical platform for simultaneous cancer-targeted imaging and magnetically guided drug delivery. *Advanced Materials,* 20, pp.478-483.

28. Chiang, C. S., Tseng, Y. H., Liao, B. J., Chen, S. Y., **2015**. Magnetically targeted nanocapsules for PAA-cisplatin-conjugated cores in PVA/SPIO shells via surfactant-free emulsion for reduced nephrotoxicity and enhanced lung cancer therapy. *Advanced Healthcare Materials,* 4, pp.1066-1075.

29. Bai, J., Wang, J. T. W., Rubio, N., Protti, A., Heidari, H., Elgogary, R., Southern, P., Al-Jamal, W. T., Sosabowski, J., Shah, A. M., Bals, S., Pankhurst, Q. A., Al-Jamal, K. T., **2016**. Triple-modal imaging of magnetically-targeted nanocapsules in solid tumours in vivo. *Theranostics,* 6(3), pp.342-356.

30. Xu, B., Dou, H., Tao, K., Sun, K., Ding, J., Shi, W., Guo, X., Li, J., Zhang, D., Sun, K., **2011**. “Two-in-one” fabrication of Fe_3O_4/MePEG-PLA composite nanocapsules as a potential ultrasonic/MRI dual contrast agent. *Langmuir,* 27, pp.12134-12142.

31. Marino, A., Arai, S., Hou, Y., Degl’ Innocenti, A., Cappello, V., Mazzolai, B., Chang, Y. -T., Mattoli, V., Suzuki, M., Ciofani, G., **2017**. Gold nanoshell-mediated remote myotube activation. *ACS Nano*. 11(3), pp.2494-2508

32. Gao, Y., Gu, J., Li, L., Zhao, W., Li, Y., **2016**. Synthesis of gold nanoshells through improved seed-mediated growth approach: brust-like, in situ seed formation. *Langmuir,* 32, pp.2251-2258.

33. Liu, X., Gao, C., Gu, J., Jiang, Y., Yang, X., Li, S., Gao, W., An, T., Duan, H., Fu, J., Wang, Y., Yang, X., **2016**. Hyaluronic acid stabilized iodine-containing nanoparticles with Au nanoshell coating for X-ray CT imaging and photothermal therapy of tumors. *ACS Applied Materials & Interfaces,* 8, pp.27622-27631.

34. Luo, L., Bian, Y., Liu, Y., Zhang, X., Wang, M., Xing, S., Li, L., Gao, D., **2016**. Combined near infrared photothermal therapy and chemotherapy using gold nanoshells coated liposomes to enhance antitumor effect. *Small,* 12(30), pp.4103-4112.

35. Wang, L., Yuan, Y., Lin, S., Huang, J., Dai, J., Jiang, Q., Cheng, D., Shuai, X., **2016**. Photothermo-chemotherapy of cancer employing drug leakage-free gold nanoshells. *Biomaterials,* 78, pp.40-49.

36. Belyanina, I. V., Zamay, T. N., Zamay, G. S., Zamay, Z. S. S., Kolovskaya, O. S., Ivanchenko, T. I., Denisenko, V. V., Kirichenko, A. K., Glazyrin, Y. E., Garanzha, I. V., Grigorieva, V. V., Shabanov, A. V., Veprintsev, D. V., Sokolov, A. E., Sadovskii, V. M., Gargaun, A., Berezovski, M. V., Kichkailo, A. S., **2017**. In vivo cancer cells elimination guided by aptamer-functionalized gold-coated magnetic nanoparticles and controlled with low frequency alternating magnetic field. *Theranostics,* 7(11), pp.2956-2967.

37. Wang, J., Xu, W., Li, S., Qiu, H., Li, Z., Wang, C., Wang, X., Ding, J., **2018**. Polylactide-cholesterol stereocomplex micelle encapsulating chemotherapeutic agent for improved antitumor efficacy and safety. *Journal of Biomedical Nanotechnology*, 14, pp.2102-2133.

38. Chen, L., Niu, D., Lee, C. H., Yao, Y., Lui, K., Ho, K. M., Li, P., **2016**. Amphiphilic core-shell nanocomposite particles for enhanced magnetic resonance imaging. *Particle & Particle System Characterization,* 33 (10), pp.756-763.

39. Ho, K. M., Li, P., **2008**. Design and synthesis of novel magnetic core-shell polymeric particles. *Langmuir,* 24, pp.1801-1807.

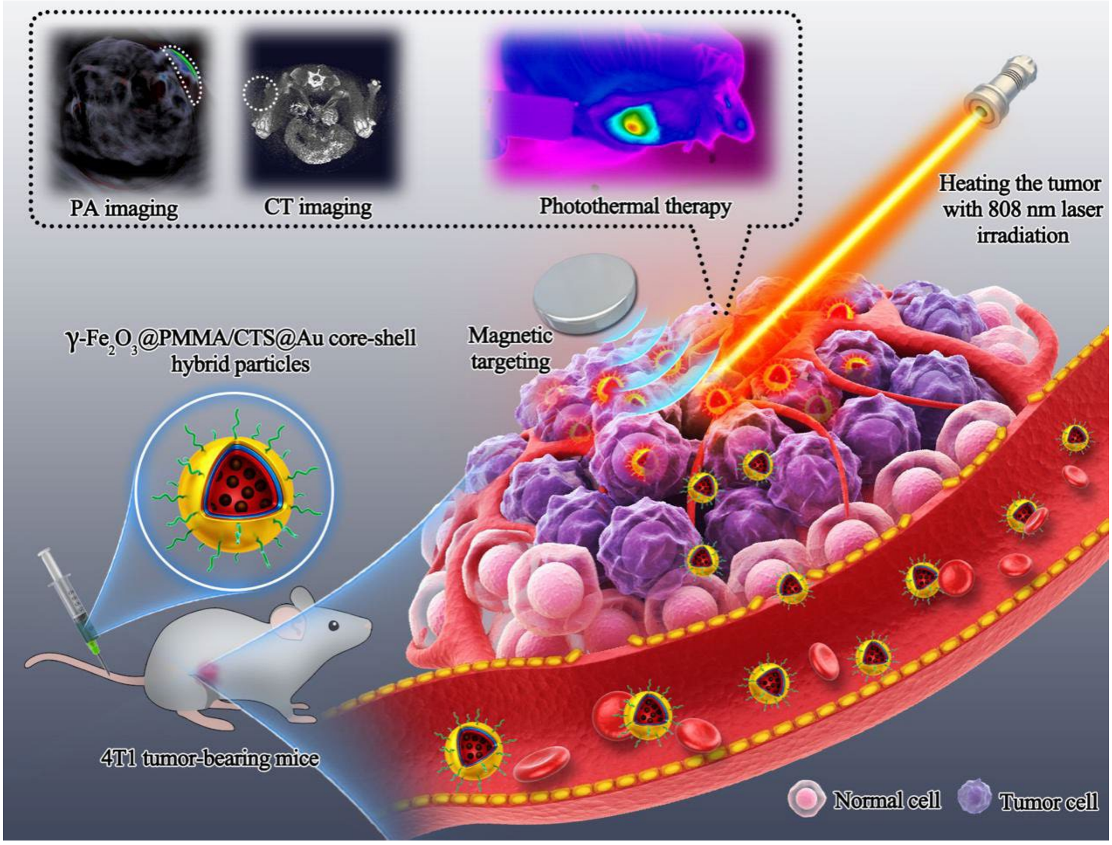

Scheme 1. An illustration of γ-Fe_2O_3@PMMA/CTS@Au core-shell hybrid particles targeting tumor region under extra-magnetic field for tumor PA/CT imaging and photothermal therapy.

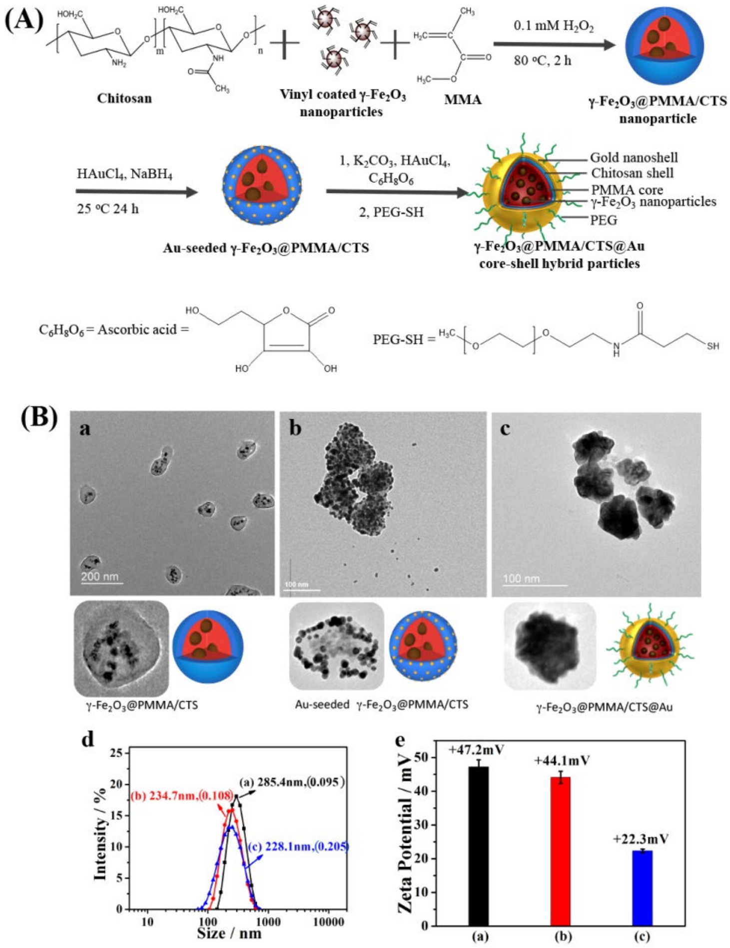

Fig. 1. (A) A synthetic scheme of γ-Fe_2O_3@PMMA/CTS@Au core-shell hybrid particles; (B) TEM images of (a) γ-Fe_2O_3@PMMA/CTS; (b) Au-seeded γ-Fe_2O_3@PMMA/CTS; (c) γ-Fe_2O_3@PMMA/CTS@Au particles; (d) The particle sizes and (e) *zeta* potentials of γ-Fe_2O_3@PMMA/CTS particles (a), Au-seeded γ-Fe_2O_3@PMMA/CTS (b) and γ-Fe_2O_3@PMMA/Au@CTS hybrid particles (c).

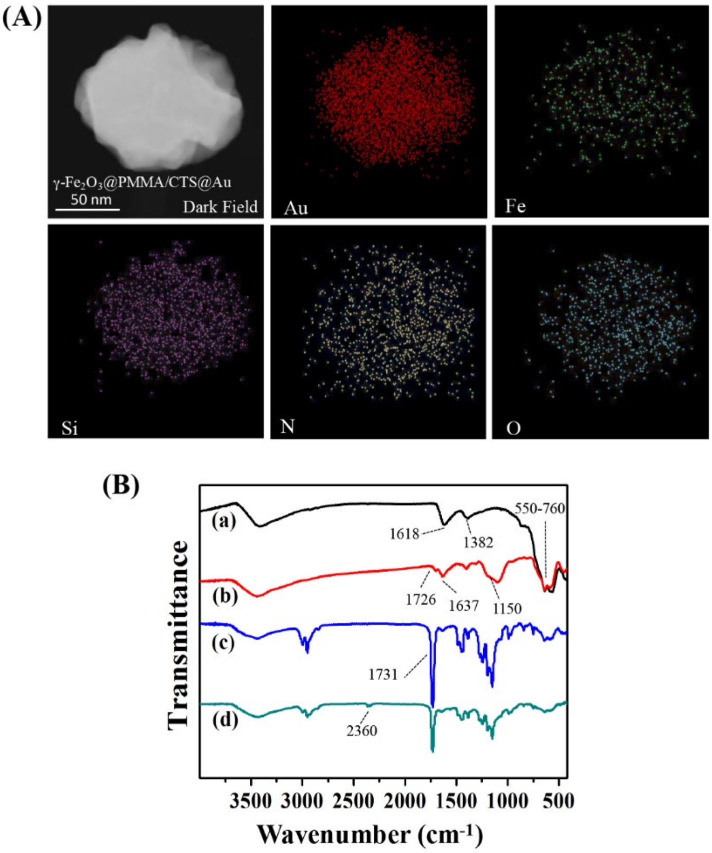

Fig. 2. (A) An energy-dispersive X-ray spectroscopy (EDS) mapping by high-angle dark-field scanning transmission electron microscopy (STEM) illustrating the representative elements and their distributions within the γ-Fe_2O_3@PMMA/CTS@Au hybrid particles; (B) FT-IR spectrum of (a) citrate-γ-Fe_2O_3, (b) MPS-γ-Fe_2O_3, (c) γ-Fe_2O_3@PMMA/CTS and (d) γ-Fe_2O_3@PMMA/CTS@Au particles.

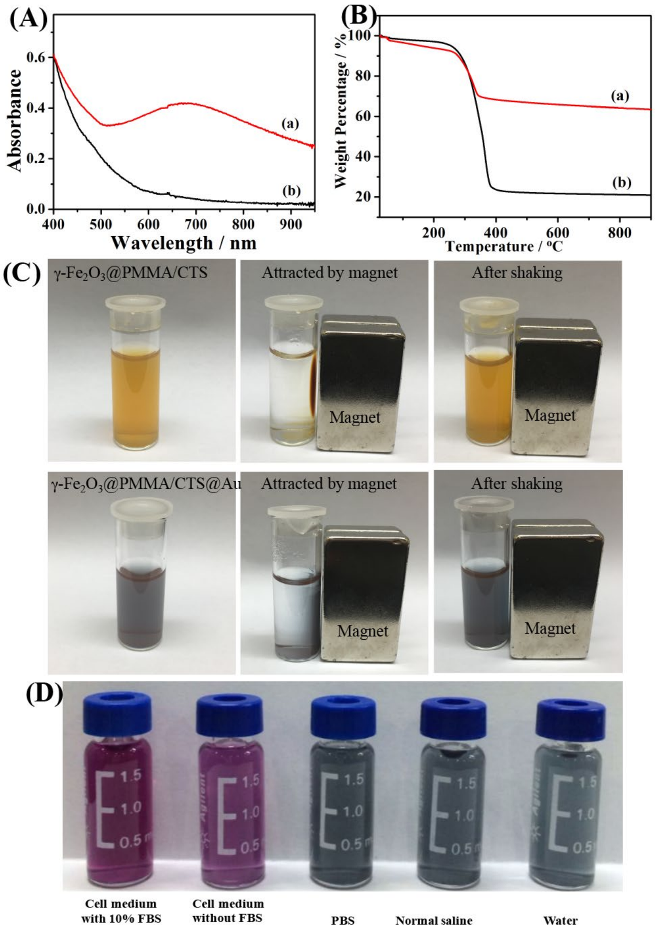

Fig. 3. (A) UV-Vis absorbance curves and (B) thermogravimetric analysis of γ-Fe_2O_3@PMMA/CTS@Au hybrid particles (a) and γ-Fe_2O_3@PMMA/CTS particles (b); (C)The magnetic responsiveness of γ-Fe_2O_3@PMMA/CTS particles and γ-Fe_2O_3@PMMA/CTS@Au hybrid particles in water; (D) The dispersions of 100 μg/mL γ-Fe_2O_3@PMMA/CTS@Au in cell medium with 10% FBS, cell medium without FBS, PBS, normal saline and water.

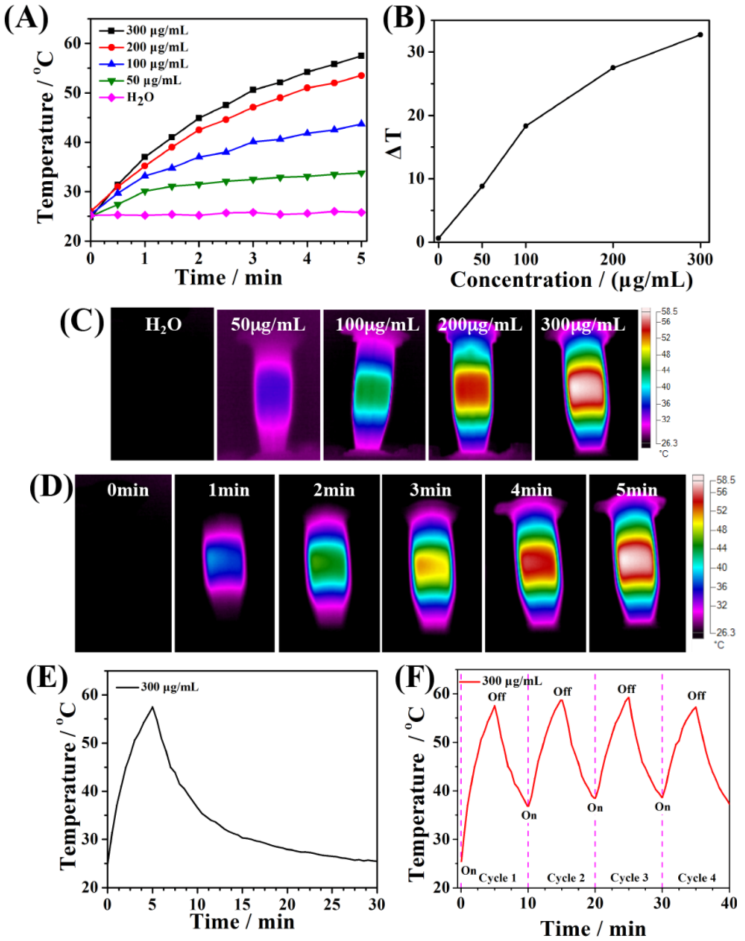

Fig. 4. (A) The temperature evaluation of γ-Fe_2O_3@PMMA/CTS@Au hybrid particles of different concentrations under 808 nm laser irradiation with a power of 3 W/cm^2; (B) A plot of temperature change over a period of 5 minutes versus the aqueous dispersion of γ-Fe_2O_3@PMMA/CTS@Au in different concentrations; (C) The IR images of γ-Fe_2O_3@PMMA/CTS@Au dispersion in different concentrations under laser irradiation recorded by an IR camera; (D) IR images of γ-Fe_2O_3@PMMA/CTS@Au dispersion with 300 μg/mL under laser irradiation at the different time recorded with an IR camera; (E) Photothermal effect of the γ-Fe_2O_3@PMMA/CTS@Au dispersion (300 μg/mL) under irradiation of an 808 nm laser which was turned off for decreasing to room temperature; (F) The temperature variation of 300 μg/mL γ-Fe_2O_3@PMMA/CTS@Au hybrid particles under 808 nm laser irradiation with a power of 3 W/cm^2 for four light on/off cycles (5 min of irradiation for each cycle).

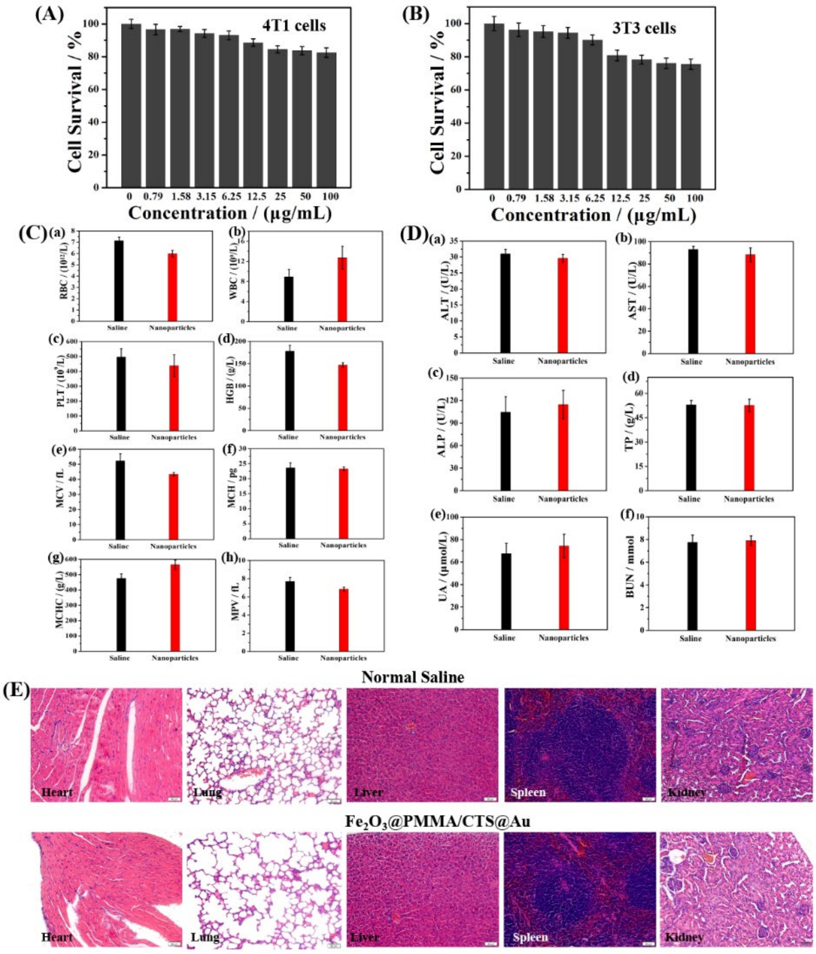

Fig. 5. *In vitro* cell viability of (A) 4T1 cells and (B) 3T3 cells incubated with γ-Fe_2O_3@PMMA/CTS@Au at various concentrations; (C) Blood hematology and (D) Blood biochemistry data of mice in the normal saline group and γ-Fe_2O_3@PMMA/CTS@Au particles treated group. (RBC: red blood cell; WBC: white blood cell; PLT: platelets; HGB: hemoglobin; MCV: mean corpuscular volume; MCH: mean corpuscular hemoglobin; MCHC: mean corpuscular hemoglobin concentration; MPV: mean platelet volume; ALT: alanine aminotransferase; AST: aspartate aminotransferase; ALP: alkaline phosphatase; TP: total protein; UA: uric acid; BUN: blood urea nitrogen); (E) H&E staining of the heart, lungs, liver, spleen, and kidneys from mice treated with normal saline and γ-Fe_2O_3@PMMA/CTS@Au, scale bar = 50 μm.

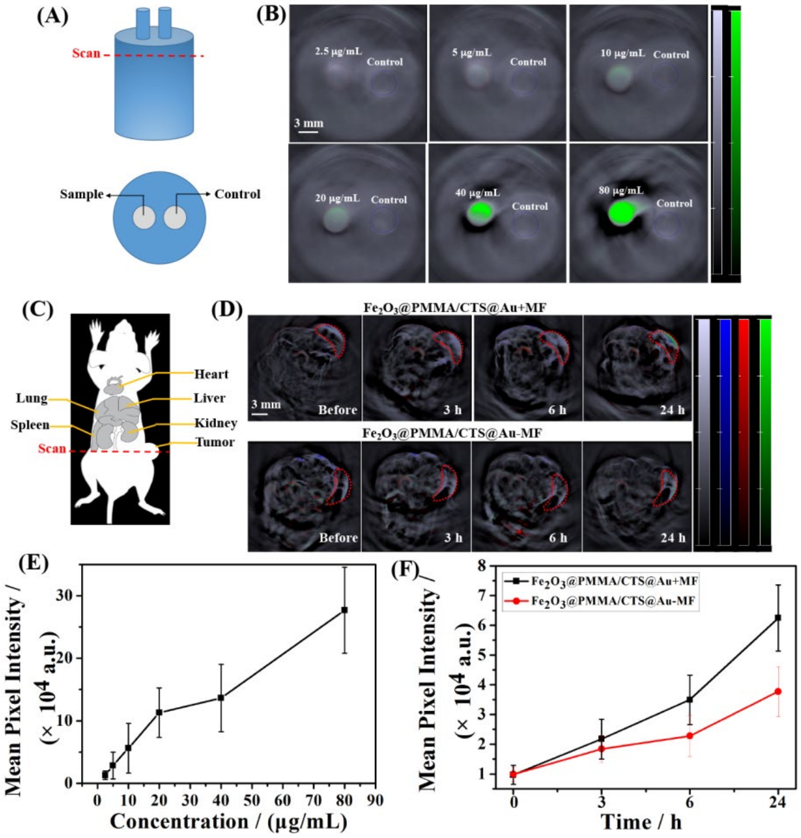

Fig. 6. (A) Elucidation of tissue-mimicking phantom setup (up), and the photoacoustic transverse image obtained at the indicated red dash line (down); (B) PA images of water as a control sample and 2.5 μg/mL, 5 μg/mL, 10 μg/mL, 20 μg/mL, 40 μg/mL, 80μg/mL of γ-Fe_2O_3@PMMA/CTS@Au dispersion; the grey bar represents the background signal, the green bar indicates the PA signal of γ-Fe_2O_3@PMMA/CTS@Au; (C) Elucidation of tumor-bearing mice scanned for PA images and the images were obtained at the indicated red dash line; (D) PA images of 4T1-bearing mice before and after intravenous injection of γ-Fe_2O_3@PMMA/CTS@Au under MF or without MF at different time intervals. The red dotted circle indicates the tumor region; the grey bar indicates the PA signal of the mice body, the blue bar indicates the PA signal of Hb, the red bar indicates the PA signal of HbO_2, and the green bar indicates the PA signal of γ-Fe_2O_3@PMMA/CTS@Au; (E) The quantitative PA signals of γ-Fe_2O_3@PMMA/CTS@Au in different concentrations; (F) The quantitative PA signal analysis in the tumor site from E.

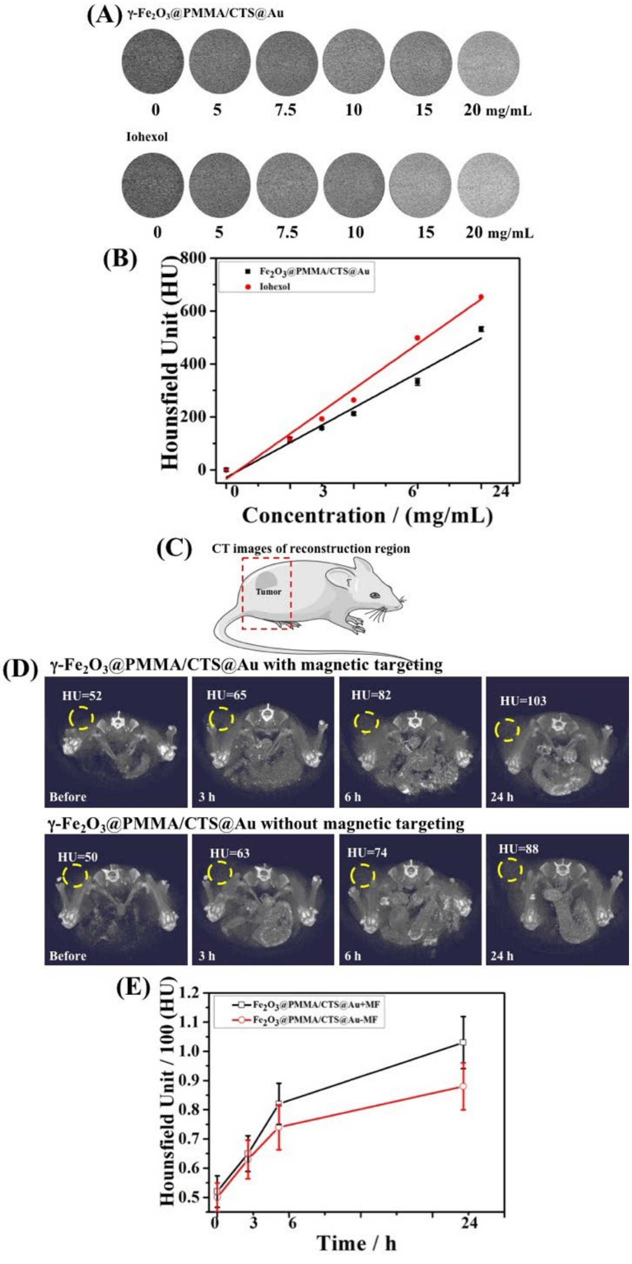

Fig. 7. (A) CT phantom images and (B) X-ray attenuation curves of γ-Fe_2O_3@PMMA/CTS@Au and Iohexol at various concentrations; (C) The illustration of the region (red square) of mice in CT reconstruction 2D images and 3D movies; (D) *In vivo* CT images and (E) the Hounsfield Unit curves of 4T1 tumor-bearing mice with or without magnetic targeting before and after administration of γ-Fe_2O_3@PMMA/CTS@Au at time points of 3, 6 and 24 h post-injection. The yellow circles point to the tumor sites.

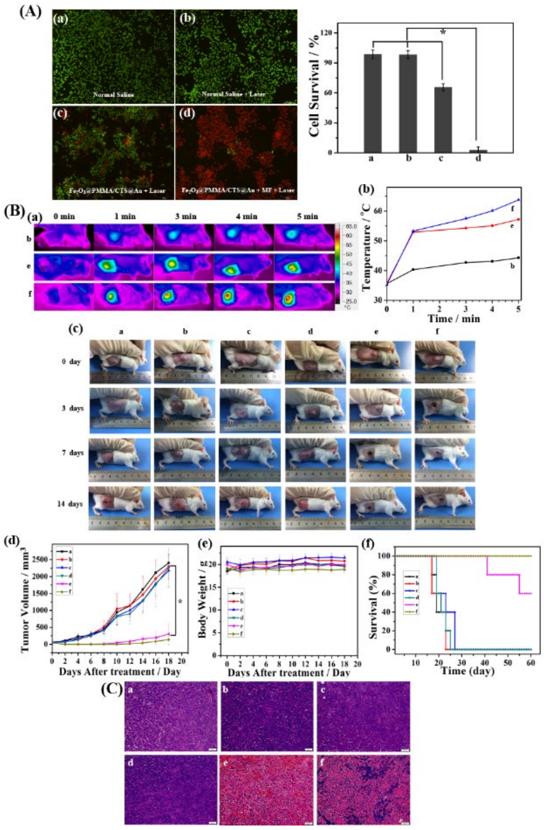

Fig. 8. (A) CLSM images of 4T1 cells incubated with normal saline without laser, with laser, γ-Fe_2O_3@PMMA/CTS@Au with laser, and γ-Fe_2O_3@PMMA/CTS@Au with laser and magnet field. All the cells are marked with calcein AM and PI; The cell viability in Group a (normal saline), b (normal saline with the laser), c (γ-Fe_2O_3@PMMA/CTS@Au with the laser), and d (γ-Fe_2O_3@PMMA/CTS@Au with laser and magnet field). (B) (a)The IR images of Group b (normal saline+Laser), Group e (γ-Fe_2O_3@PMMA/CTS@Au+Laser), and Group f (γ-Fe_2O_3@PMMA/CTS@Au+MF+Laser) under laser irradiation (808 nm, 3.0 W/cm^2) at the different time recorded with an IR camera; (b) The temperature curves of the tumor regions of different groups at 0 min, 1 min, 3 min, 4 min, and 5 min; (c) The photographed images, (d) Growth curves, (e) The body weight curves and (f) Survival curves of 4T1 tumors on mice of Group a (normal saline), Group b (normal saline+Laser), Group c (γ-Fe_2O_3@PMMA/CTS@Au), Group d (γ-Fe_2O_3@PMMA/CTS@Au+MF), Group e (γ-Fe_2O_3@PMMA/CTS@Au+Laser) and Group f (γ-Fe_2O_3@PMMA/CTS@Au+MF+Laser) after corresponding treatments as indicated (n = 5). (C) H&E staining of tumor tissues of mice after different treatments for 2 days, scale bar = 50 μm.

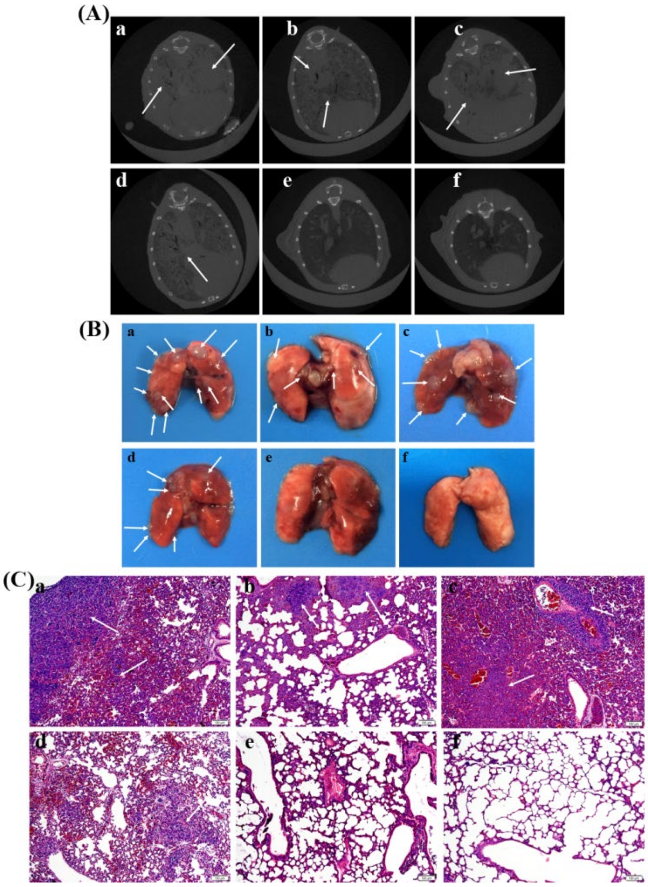

Fig. 9. (A) The 2D reconstruction images of 4T1 tumor-bearing mice, (B) Lung tissues, and (C) H&E staining of the lung tissues obtained from Group a (normal saline), Group b (normal saline+Laser), Group c (γ-Fe$_2$O$_3$@PMMA/CTS@Au), Group d (γ-Fe$_2$O$_3$@PMMA/CTS@Au+MF), Group e (γ-Fe$_2$O$_3$@PMMA/CTS@Au+Laser) and Group f (γ-Fe$_2$O$_3$@PMMA/CTS@Au+MF+Laser) after different treatments for 28 days; The white arrows indicated the regions of tumor metastasis regions, scale bar = 100 μm.